analytical chemistry

pubs.acs.org/ac Article

Ultrasensitive Double-Channel Microfluidic Biosensor-Based Cathodic Photo-electrochemical Analysis via Signal Amplification of SOD-Au@PANI for Cardiac Troponin I Detection

Jinhui Feng,[§] Ning Li,[§] Yu Du,* Xiang Ren, Xueying Wang, Xuejing Liu, Hongmin Ma,* and Qin Wei

Cite This: *Anal. Chem.* 2021, 93, 14196−14203 Read Online

ACCESS | Metrics & More | Article Recommendations | Supporting Information

ABSTRACT: Interesting double-channel microfluidic chip integration with a sandwich-type cathodic photo-electrochemical (PEC) biosensor is utilized for ultrasensitive and efficient detection of cardiac troponin I (cTnI) based on a signal amplification strategy. The Pd nanoparticles loading on the I-doped bismuth oxybromide with oxygen vacancies (Pd/I:BiOBr-OVs) as a sensing platform can effectively enhance cathodic photocurrent response by improving the visible light absorption ability with I doping, facilitating the efficiency separation of photogenerated electron−hole pairs with OVs, and increasing the electron-transfer rate with Pd loading, where the photogenerated electron could be captured by dissolved O_2 to boost generation of a superoxide anion radical ($^{\bullet}O_2^-$). To further enhance the PEC response, a novel superoxide dismutase loaded on gold@polyaniline (SOD-Au@PANI) as a signal amplification label is developed for incubating the detection antibody (dAb). It is particularly noteworthy that SOD can effectively catalyze dismutation of the $^{\bullet}O_2^-$ to produce H_2O_2 and O_2, and Au@PANI with a good reduction and catalytic property can catalyze the produced H_2O_2 into H_2O and O_2. Then, the produced O_2 that has been dissolved or adsorbed can capture more photogenerated electrons, resulting in more electron−hole pairs to separate, so as to the cathodic photocurrent signal of this system which can be amplified more significantly. Therefore, a signal amplification cathodic PEC biosensor is prepared for sensitively detecting cTnI, in which a good linearity ranging from 0.1 pg/mL to 100 ng/mL with a low detection limit of 0.042 pg/mL is obtained. Furthermore, the proposed biosensor exhibits excellent sensitivity and high selectivity, which could be extended to detect other disease markers in biological analysis and early disease diagnosis.

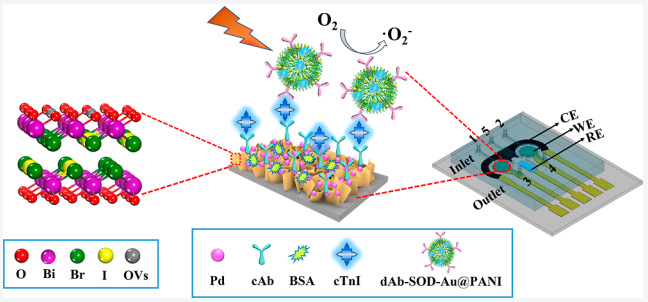

1. INTRODUCTION

As a newly emerged and promising analytical technique for testing biomarkers, the photo-electrochemical (PEC) biosensor has aroused great attention owing to its attractive merits of high sensitivity, low background signal, easy operation, and low cost.[1−3] However, the lack of portability limits PEC biosensor application for point-of-care detection. To overcome this obstacle, the microfluidic chip structure with miniaturization, less sample consumption, good portability, and short analysis time is introduced to integrate with the PEC biosensor, which provides a new strategy for the construction of miniature portable sensors with high sensitivity.[4−6] In general, PEC biosensors can be divided into photocathode biosensors and photoanode biosensors. Interestingly, the photocathode biosensors not only possess excellent merits of the PEC biosensor but also can resist the interference of reducing substances because it could react with electron acceptors (e.g., dissolved O_2).[7,8] In addition, the cathodic PEC biosensor represents the latest development direction in this field. Therefore, it is an urgent demand to combine the highly sensitive cathodic PEC biosensor with a portable microfluidic chip.

Indeed, the sensitivity of the PEC biosensor largely relies on the photon-to-electron conversion efficiency of semiconductor photosensitive materials, which directly guarantee the signal output and determine the intensity of photocurrent. Nowadays, explosive kinds of photoactive materials, such as metal oxide semiconductors (ZnO, TiO_2, and CuO),[9−11] sulfide semiconductors ($CuInS_2$, PbS, CdS, and Ag_2S),[12−14] and different kinds of heterojunction structures (AgI/$Bi_2Ga_4O_9$, α-Fe_2O_3/g-C_3N_4, and AgI/Ag/BiOI),[15−17] have been employed to improve PEC response. Particularly, the p-type semiconductor material with holes as the major carriers has been widely used in the cathodic PEC biosensor. A typical p-type semiconductor material of bismuth oxyhalides (BiOX, X = Cl, Br, and I) has drawn tremendous attention in the fields of water splitting, organic pollutant degradation, CO_2 reduction,

Received: July 12, 2021
Accepted: September 27, 2021
Published: October 12, 2021

https://doi.org/10.1021/acs.analchem.1c02922
Anal. Chem. 2021, 93, 14196−14203

Scheme 1. Schematic Process of the dAb-SOD-Au@PANI Bioconjugate (A) and Presentation of the Fabricated Sandwich-Type Cathodic PEC Biosensor in a Double-Channel Microfluidic Chip for cTnI Detection (B)

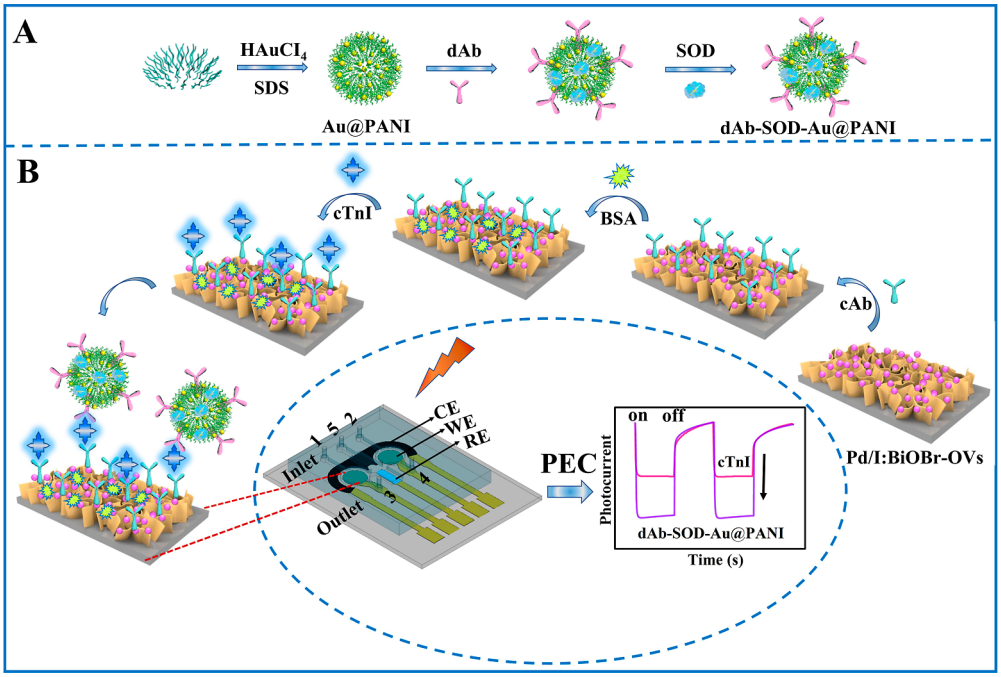

and PEC biosensors because of its outstanding photocatalytic activity.[18−20] Among them, BiOBr reveals excellent photocatalytic activity under visible light irradiation due to its suitable band gap energy (~2.7 eV), unique laminar structure with alternatively arranged double bromine ion layer and $[Bi_2O_2]^{2+}$ layer, and chemical stability.[21,22] Nevertheless, low visible light utilization still limits the practical application. Iodine doping is considered to be an effective way to expand the visible light absorption range and reduce band gap energy of BiOBr by forming I^- impurity levels.[23] However, a smaller band gap energy of I-doped BiOBr (I:BiOBr) also makes recombination of photoinduced electrons and holes easier. To address this, it is of great significance to introduce surface oxygen vacancies (OVs) with abundant localized charge density and coordinatively unsaturated nature in I:BiOBr, which can effectively improve the separation of photoinduced electron−hole pairs for developing highly efficient photoelectric conversion.[24,25] Meanwhile, the OVs facilitate the adsorption of O_2 acting as electron acceptors, which is very necessary for photocathodic biosensor application. Moreover, loading Pd precious metal nanoparticles on a semiconductor is another effective strategy to improve PEC photocurrent. The loaded metal nanoparticles can not only perform electron traps to accelerate charge transfer at the interface but also provide sites for expediting the activation of O_2 for capturing electrons to form superoxide radicals ($^{\bullet}O_2^-$).[26] The coexistence of OVs and Pd on the surface of I:BiOBr can more effectively accelerate the separation rate of photogenerated electron−hole pairs and improve photocurrent response.

To further achieve an amplification signal and enhance the sensitivity of the cathodic PEC biosensor, one of the most popular strategies is to build a sandwich-type biosensor. For a cathodic PEC biosensor, the photoinduced electrons could be captured by O_2 (dissolved O_2 or absorbed O_2) to form $^{\bullet}O_2^-$ that if consumed, facilitates the efficiency separation of electron−hole pairs to enhance the cathodic PEC signal. Superoxide dismutase (SOD), a good scavenger of superoxide free radicals, can effectively catalyze the dismutation of $^{\bullet}O_2^-$ to H_2O_2 and O_2. Fortunately, the generated H_2O_2 could be catalyzed to form H_2O and O_2 by Au@PANI that has a good reduction property toward H_2O_2 and significant electron-transfer ability. Moreover, the produced O_2 can be further dissolved in the electrode solution or absorbed on the surface of OVs, which can trap the more photoinduced electrons for achieving an amplification signal.

Herein, a highly sensitive cathodic PEC biosensor integrated with a portable microfluidic chip has been proposed for biomarker detection using a photoactive material of Pd/I:BiOBr-OVs as a sensing platform for immobilizing the capture antibody (cAb) and SOD-Au@PANI as a multiple signal amplification label for marking detection antibody (dAb). Here, cardiac troponin I (cTnI) was selected as a model because it is a reliable biomarker of acute myocardial infarction. As expected, the Pd/I:BiOBr-OVs improve photocurrent response by enhancing visible light absorption ability, promoting efficiency separation of photogenerated electron−hole pairs, and increasing the electron-transfer rate. What is more, the Pd/I:BiOBr-OVs increase the generation rate of $^{\bullet}O_2^-$ that is produced by photogenerated electrons capturing O_2. Then, the SOD-Au@PANI serving as a signal amplification label can catalyze the decomposition of $^{\bullet}O_2^-$ to produce O_2. Subsequently, the produced O_2 can be dissolved or adsorbed for the reduction of photogenerated electrons to improve the separation of electron−hole pairs so as to the fact that the cathodic photocurrent signal of this system can be amplified more significantly. Besides, traditional preparation of a working electrode can only detect one target concentration; here, a double-channel microfluidic working electrode is designed to improve the detection efficiency of the PEC biosensor in this work. Therefore, the developed double-channel microfluidic cathodic PEC biosensor can not only sensitively detect cTnI but also easily expand to detect other disease biomarkers.

https://doi.org/10.1021/acs.analchem.1c02922
Anal. Chem. 2021, 93, 14196−14203

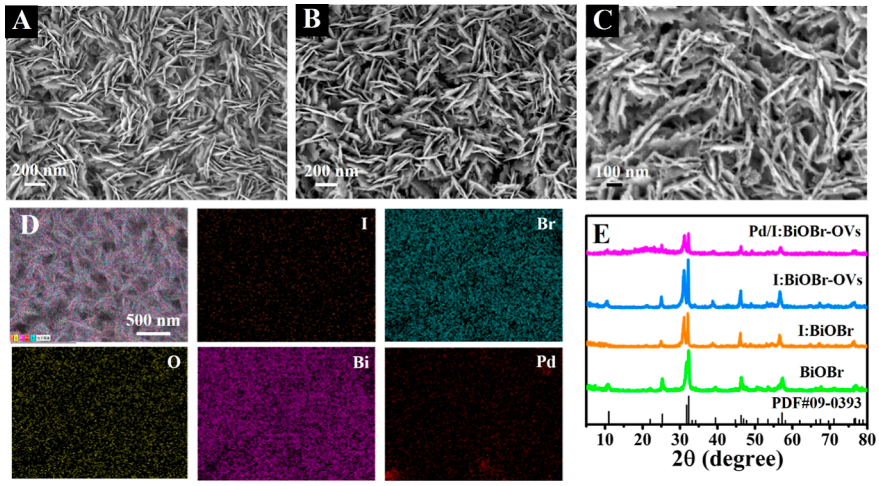

Figure 1. SEM images of I:BiOBr (A), I:BiOBr-OVs (B), and Pd/I:BiOBr-OV nanocomposite (C); SEM elemental mapping of the Pd/I:BiOBr-OV nanocomposite (D); and XRD pattern of BiOBr, I:BiOBr, I:BiOBr-OVs, and Pd/I:BiOBr-OVs (E).

2. EXPERIMENTAL SECTION

2.1. Double-Channel Microfluidic Chip with Three-Electrode System Fabrication. The microelectrode of two working electrodes (WE1 and WE2) was obtained by wet etching of ITO, and the details are shown in Figure S1. Following this, the counter electrode and reference electrode were gained by silk screen printing of carbon paste screen and Ag−AgCl conductive ink, respectively (Figure S1). The double-channel microfluidic template and the isolation membrane template were fabricated via the soft lithography method, whose pattern design was employed using Auto CAD. The isolation membrane (Figure S2A) and the double-channel microfluidic template (Figure S2B) were prepared using poly(dimethylsiloxane) (PDMS: curing agent and base agent in a weight ratio of 1:10). Finally, the PDMS of the isolation membrane and the double-channel microfluidic film were attached to the designed three-electrode system to gain double-channel microfluidic chip electrodes (Figure S2C).

2.2. Preparation of Pd/I:BiOBr-OVs. First, the I:/BiOBr was prepared by template-free self-assembly on the WE. 1 mmol $Bi(NO_3)_3{\cdot}5H_2O$ was dissolved in 7.5 mL of glycol to obtain the Bi precursor and 0.25 mmol KI with 0.75 mmol NaBr were dissolved in 12.5 mL of ultrapure water to gain Br with an I precursor. Then, the Bi precursor solution of 200 μL was injected into WE1 and WE2 (from inlet 1 and 2), respectively, then outflowed them from outlet 3 and 4 after reacting for 3 min. After that, the Br with I solution of 200 μL was also injected into WE1 and WE2 (from inlet 1 and 2) and reacted for another 3 min. The I:BiOBr was obtained after repeating 10 times and washing. The OVs for I:BiOBr was gained by reducing the reagent of glyoxal under relatively low temperature. In detail, the 0.08 mmol/L 200 μL of glyoxal solution was injected into WE1 and WE2 (from inlet 1 and 2) and reacted for 6 h at 80 °C on the heating plate. The I:BiOBr-OVs were obtained after washing. The Pd was loaded on the surface of I:BiOBr-OVs according to our previous work.[27] The 0.2 mol/L 400 μL of sodium tetrachloropalladate(II) was injected into WE and holded for 1 h to make palladium ions adsorb on the I:BiOBr-OVs surface. Then, the sodium borohydride solution was injected into WE for the in situ reduction of Pd for gaining the Pd/I:BiOBr-OVs nanocomposite.

2.3. Preparation of dAb-SOD-Au@PANI Conjugates. To prepare Au@PANI nanoparticles as shown in Scheme 1A, $HAuCl_4$ (2.94 mM, 4 mL), aniline (100 mM, 4 mL), and sodium dodecylsulfate (40 mM, 4 mL) were mixed and shaked for 10 min. Then, 4 mL of ultrapure water was added to the abovementioned solution drop by drop and incubated for 4 h at room temperature. Then, Au@PANI was obtained by washing and drying overnight at 60 °C. After that, the Au@PANI (3 mL, 1 mg/mL) was incubated with SOD solution (500 μL, 0.5 mg/mL) and dAb solution (1 mL, 10 μg/mL) overnight at 4 °C. Finally, the obtained dAb-SOD-Au@PANI conjugates were washed and redispersed in PBS for future use.

2.4. Fabrication of a Double-Channel Microfluidic PEC Biosensor for cTnI Detection. The fabricated sandwich-type cathodic PEC biosensor in a double-channel microfluidic chip for cTnI detection is presented in Scheme 1B. First, the cAb solution (20 μL, 5 μg/mL) was injected ino Pd/I:BiOBr-OV WE1 and Pd/I:BiOBr-OV WE2 (from inlet 1 and 2) and holded for 60 min to achieve Pd−NH_2 linking between the cAb and Pd/I:BiOBr-OV nanocomposite. Next, the BSA solution (10 μL, 1 mg/mL) was injected into the abovemodified WE to block nonspecific binding sites. Then, the cTnI (20 μL) with different concentrations was injected into BSA/cAb/Pd/I:BiOBr-OV WE1 and BSA/cAb/Pd/I:BiOBr-OV WE2 from inlet 1 and 2 and incubated for 60 min. Subsequently, the 20 μL of dAb-SOD-Au@PANI was injected (from inlet 1 and 2) and incubated for 60 min. Then, the cathodic photocurrent is greatly increased after the modification of dAb-SOD-Au@PANI compared with modifying cTnI to achieve signal amplification. Each modification step was cleaned with PBS buffer solution (pH 7.4) to remove unabsorbed biomolecules, in which the solution was injected from inlet 1 and 2 and then outflowed from outlet 3 and 4. The physical picture of a double-channel microfluidic chip biosensor is shown in Figure S3.

3. RESULTS AND DISCUSSION

3.1. Characterization of Pd/I:BiOBr-OVs and Au@PANI. The morphologies of I:BiOBr, I:BiOBr-OVs, and Pd/I:BiOBr-OVs were characterized by SEM. As shown in Figure 1A, I:BiOBr nanomaterials are nanosheet arrays with the self-assembled unordered flower-like surface, indicating the successful preparation of I-doped BiOBr. After OVs for

https://doi.org/10.1021/acs.analchem.1c02922
Anal. Chem. 2021, 93, 14196−14203

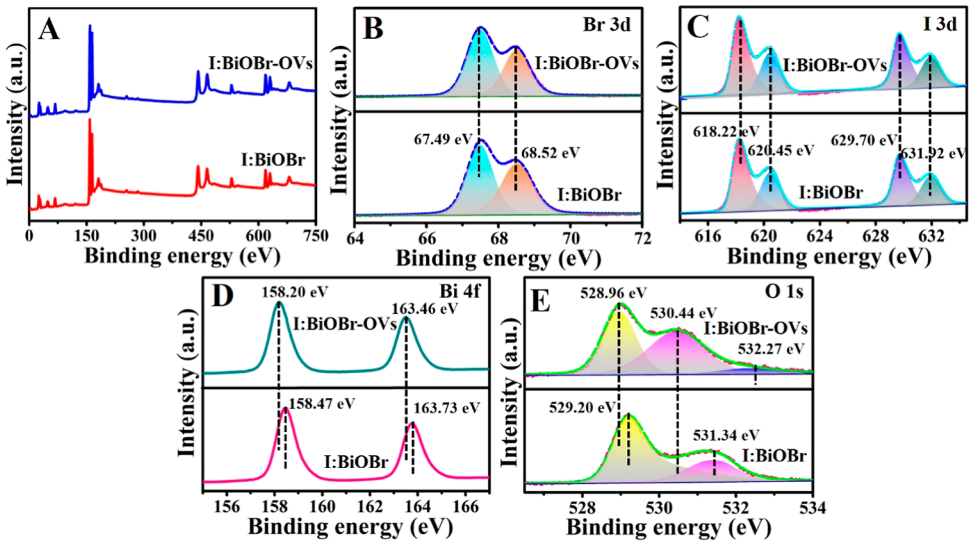

Figure 2. XPS spectra of I:BiOBr and I:BiOBr-OVs (A); Br 3d (B); I 3d (C); Bi 4f (D); and O 1s (E).

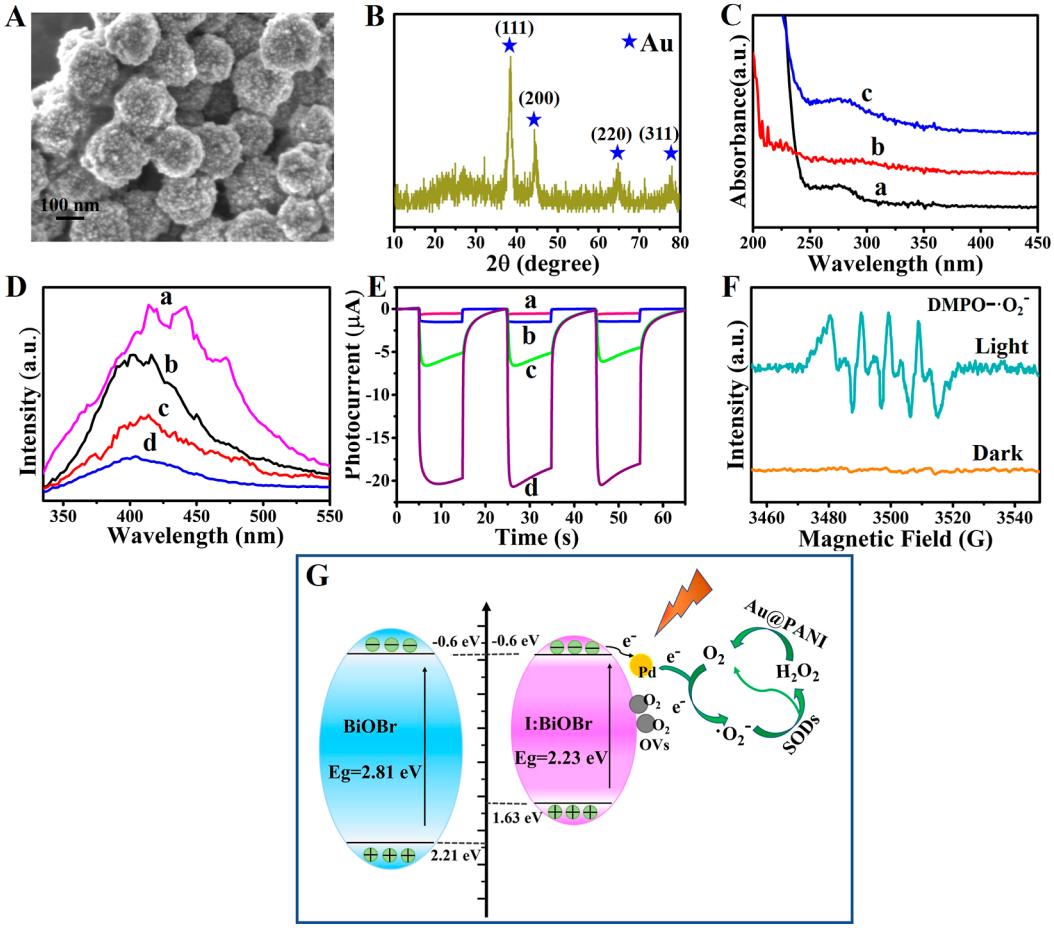

Figure 3. SEM images of Au@PANI (A); XRD pattern of Au@PANI (B); UV−vis spectra of (a) dAb, (b) Au@PANI, and (c) dAb-Au@PANI (C); PL spectra (D) and photocurrent intensity (E) of (a) BiOBr, (b) I:BiOBr, (c) I:BiOBr-OVs, and Pd/I:BiOBr-OVs; ESR spectra of $^{\bullet}O_2^-$ radicals produced by Pd/I:BiOBr-OVs in the dark and under visible light photoirradiation (F); and possible signal amplification mechanism (G).

I:BiOBr (Figure 1B), the nanosheet array becomes loose and the edge of the nanosheet is damaged, which was most likely caused by surface OVs. Importantly, nanosheet arrays can provide more reaction sites over a larger specific surface area and improve the stability of the signal. After loading Pd nanoparticles on I:BiOBr-OVs by in situ reduction, as shown in Figure 1C, the Pd nanoparticles are uniformly loaded on the surface of I:BiOBr-OVs whose morphology has little change. In addition, the high-resolution transmission electron microscopy (HRTEM) image of Pd nanoparticles (Figure S4) presents the lattice fringes with 0.23 nm corresponding to the spacing of (111) planes in cubic Pd. Moreover, the elements of I, Br, O,

https://doi.org/10.1021/acs.analchem.1c02922
Anal. Chem. 2021, 93, 14196−14203

Bi, and Pd are uniformly distributed on the Pd/I:BiOBr-OV sample in Figure 1D, which further indicates the successful synthesis of Pd/I:BiOBr-OV composites. The X-ray diffraction (XRD) pattern was employed to characterize the crystallinity of the prepared I:BiOBr, I:BiOBr-OVs, and Pd/I:BiOBr-OV nanocomposite, respectively. As shown in Figure 1E, the diffraction peaks in the XRD pattern for BiOBr, I:BiOBr, and I:BiOBr-OVs are well-indexed to the standard card of tetragonal BiOBr (JCPDS 09-0393), showing the introduction of I doping and OVs that do not alter the crystalline phase of BiOBr. However, a main diffraction peak at 2θ = 31.69 (102) for I:BiOBr and I:BiOBr-OVs is shifted a little bit to a lower angle area, which is most probably caused by doping of I ions into the BiOBr lattice structure. All the diffraction peaks weaken when Pd nanoparticles are loaded on the I:BiOBr-OV surface, meaning a successful reduction of Pd nanoparticles on the I:BiOBr-OV surface.

XPS was employed to investigate surface atomic constituents and chemical states of elements for I:BiOBr and I:BiOBr-OVs. The elements of Br, Bi, O, and I are all in full XPS survey spectra of I:BiOBr and I:BiOBr-OVs, as shown in Figure 2A. The same two diffraction peaks at 67.49 and 68.52 eV (Figure 2B) for I:BiOBr and I:BiOBr-OVs are associated with Br $3d_{5/2}$ and Br $3d_{3/2}$, respectively, revealing the existence of Br^-. Figure 2C shows that the two same high-resolution spectra of I $3d_{5/2}$ and I $3d_{3/2}$ with peaks at 618.22 and 629.70 eV for I:BiOBr and I:BiOBr-OVs, respectively, are assigned to I 3d. In addition, the existence of a weak diffraction peak at 620.45 and 631.92 eV for I 3d may be caused by air oxidation. The strong typical characteristic peaks at 158.47 and 163.73 eV (Figure 2D) for I:BiOBr are assigned to Bi $4f_{7/2}$ and Bi $4f_{5/2}$, respectively. However, there is an obvious 0.27 eV shift to lower binding energy for the Bi 4f spectrum in I:BiOBr-OVs, which was caused by OVs that break the Bi−O bond. The O 1s spectrum of I:BiOBr and I:BiOBr-OVs is displayed in Figure 2E. Compared to I:BiOBr with two main diffraction peaks at 531.34 and 529.2 eV from lattice −OH and Bi−O, respectively, the O 1s diffraction peak of I:BiOBr-OVs shifts to lower binding energy (528.96 and 530.44 eV) and a new peak appears at 532.27 eV, which attributed to the treatment of OVs on the I:BiOBr surface.[28,29] Therefore, the I:BiOBr samples with OVs have been successfully prepared.

The morphology of Au@PANI was characterized by SEM, as shown in Figure 3A. Also, Au@PANI presents a nanoparticle shape in uniform size with an average diameter of 200 ± 10 nm. In addition, the crystalline phase of Au@PANI was analyzed by the XRD pattern. As shown in Figure 3B, four intense absorption peaks exhibit at 38.2, 44.4, 64.6, and 77.5° corresponding to reflection planes of (111), (200), (220), and (311), respectively, which represents the face-centered cubic structure of Au nanoparticles. At the same time, a broad diffraction peak was observed between 20 and 30°, which confirms the amorphous characteristics of PANI.[30] Therefore, the XRD pattern proved that the Au@PANI nanomaterial was synthesized successfully. In addition, the UV−vis spectrum was used to identify incubation connection of dAb with Au@PANI, as shown in Figure 3C. The dAb dispersion has an obvious absorption peak (curve a) at 273 nm. Subsequently, a small peak (curve b) at 300 nm is observed for Au@PANI aqueous solution. After incubation, it can detect a relatively strong peak (curve c) at 273 nm obviously, which mainly ascribed to the successful connection of dAb with Au@PANI.

Photoluminescence (PL) spectra are usually used to test efficiency separation of photoinduced electron−hole pairs. Also, the lower PL intensity suggested the higher charge separation efficiency.[31,32] As shown in Figure 3D, PL spectra of BiOBr, I:BiOBr, I:BiOBr-OVs, and Pd/I:BiOBr-OVs show that all the samples have wide emission peaks around 350−475 nm. In addition, the peak intensity of I:BiOBr (curve b) is obviously weaker than that of pure BiOBr (curve a), indicating that I^- doping could improve the separation rate of electron−hole pairs. Interestingly, the peak intensity of I:BiOBr-OVs (curve c) is reduced compared with that of I:BiOBr, which was caused by the introduction of OVs that greatly promote the separation of photogenerated carriers. It is worth noting that the PL peak intensity of Pd/I:BiOBr-OVs (curve d) is the lowest because loading Pd on I:BiOBr-OVs could further inhibit the recombination of photoinduced electron−hole pairs.[26] Besides, the intensity of photocurrent could reflect the situation of photogenerated electrons. As shown in Figure 3E, the photocurrent intensity of I:BiOBr (curve b) increases than that of BiOBr (curve a) and further enhances with the introduction of OVs on the surface of I:BiOBr (curve c). The enhanced photocurrent intensity may be caused by two factors, one is the increase in photoinduced charge carrier quantity and another is improvement of electron−hole pair separation efficiency. The intensity photocurrent of I:BiOBr-OVs increased obviously after loading Pd nanoparticles (curve d) that mainly increase the electron-transfer rate. The photocurrent response data corresponded with PL spectral values, which confirmed that Pd/I:BiOBr-OVs has good PEC properties.

3.2. Possible Signal Amplification Mechanism of the Biosensor. To acquire a deeper understanding of the enhanced PEC response based on Pd/I:BiOBr-OVs as a platform and SOD-Au@PANI as a signal amplification label. The possible mechanism was proposed and is presented in Figure 3G. First, the conduction band (CB) and valence band (VB) edges were studied by linear sweep voltammetry (LSV): the CB edge and the VB edge of BiOBr are at −0.80 V (Figure S5A) and 2.01 V (Figure S5B) versus Ag/AgCl electrode, corresponding to −0.60 and 2.21 V, respectively, as opposed to the normal hydrogen electrode (NHE). Also, the CB edge and VB edge of I:BiOBr are at −0.60 and 1.63 V (Figure S6A,B) versus NHE by calculations from LSV measurements. According to the following equation, the calculated band gap (E_g) of BiOBr and I:BiOBr is 2.81 and 2.23 eV, respectively. The E_g of BiOBr becomes narrower after I doping, leading to the promotion of a wider visible-light absorption range and generation of more pairs of separated electrons and holes.

$$E_g = E_{VB} - E_{CB}$$

Then, upon visible-light irradiation for Pd/I:BiOBr-OVs, the electron (e^-) could be excited and jumped to the CB of I:BiOBr or OV states and holes (h^+) could be left in the VB to occur separation of electron−hole pairs (eq 1). The e^- on the CB of I:BiOBr could transfer to the Pd surface that provide more reactive sites to facilitate the separation of electron−hole pairs; meanwhile, the e^- with a redox potential of −0.60 V can be captured by dissolved O_2 to produce $^{\bullet}O_2^-$ radicals [$E^0(O_2/^{\bullet}O_2^-$ = −0.33 V/NHE)] (eq 2). On top of that, the e^- also could be captured by absorbed O_2 on the OV surface to generate $^{\bullet}O_2^-$ radicals (eq 2). It is interesting to note that the generated $^{\bullet}O_2^-$ radicals in the PEC reaction can be identified by electron spin resonance (ESR) spectroscopy, which used

https://doi.org/10.1021/acs.analchem.1c02922
Anal. Chem. 2021, 93, 14196−14203

DMPO as a spin-trapping agent. As shown in Figure 3F, the sample of Pd/I:BiOBr-OVs exhibited the highest ESR signal for $^{\bullet}O_2^-$ radical generation under visible-light irradiation, while the ESR signal was hardly observed under dark conditions, suggesting that the $^{\bullet}O_2^-$ radicals could be produced in the PEC reaction system.[33,34] In addition, the $^{\bullet}O_2^-$ could disproportionate with SOD on the label of dAb-SOD-Au@PANI to produce O_2 and H_2O_2, leading to further facilitation of the separation of electron−hole pairs (eq 3). Hence, the cathodic PEC response is amplified by promoting the e^- consumption reaction. More interestingly, the produced H_2O_2 can be catalyzed by Au@PANI to generate O_2 and H_2O (eq 4). Finally, the generated O_2 increases the content of dissolved O_2 and adsorbed O_2, which can capture more e^-. Therefore, the label of SOD-Au@PANI could further amplify PEC response through efficient separation of electron−hole pairs.

$$\text{Pd/I:BiOBr-OVs} + h\vec{\nu} \rightarrow \text{Pd/I:BiOBr-OVs}(e^- + h^+) \quad (1)$$

$$e^- + O_2 \rightarrow {}^{\bullet}O_2^- \quad (2)$$

$${}^{\bullet}O_2^- + 2H^+ \xrightarrow{\text{SOD}} O_2 + H_2O_2 \quad (3)$$

$$H_2O_2 \xrightarrow{\text{Au@PANI}} O_2 + H_2O \quad (4)$$

3.3. Increased Electroactive Surface Area of Pd/I:BiOBr-OVs. The effective electroactive surface area was enhanced by the introduction of Pd loading on the surface of I:BiOBr-OVs that with the unordered flower-like nanosheet arrays are key to establish electron transport and amplify PEC signals with faster electron mobility. To illustrate that, the CV of pure WE and Pd/I:BiOBr-OVs WE was studied in $[Fe(CN)_6]^{4-/3-}$ solution. The redox peak current I was related to $\nu^{1/2}$, according to the Randles−Sevcik equation

$$I = 2.69 \times 10^5 A D^{1/2} n^{3/2} \nu^{1/2} c$$

where A is the effective electroactive surface area (cm^2), D represents the diffusion coefficient of $[Fe(CN)_6]^{4-/3-}$, n is 1, ν is the scanning rate (V/s), and c is 5 mmol/L that represents the concentration of $K_3Fe(CN)_6$. Under scanning rates from 40 to 240 mV/s (Figure S7A), the current I increases linearly with $\nu^{1/2}$ for pure WE and the regression equation is presented as $I = 922.28 \times \nu^{1/2} + 176.86$ ($R^2 = 0.992$) (Figure S7B). The calculated effective electroactive surface area is 0.26 cm^2. However, the effective electroactive surface area of Pd/I:BiOBr-OVs increased to 0.58 cm^2 by calculation with regression equations of $I = 2038.63 \times \nu^{1/2} + 231.24$ ($R^2 = 0.996$) (Figure 4A) along with scanning rates from 40 to 240 mV/s (the inset in Figure 4A). The results demonstrate that Pd/I:BiOBr-OVs possessed increasing effective electroactive surface area.

3.4. EIS Characterization of the PEC Biosensor. The interfacial properties of each construction step were expressed by an effective way of EIS. As shown in Figure 4B, the inset is an equivalent circuit containing R_{et} (electron-transfer resistance), Z_w (Warburg impedance), C_{dl} (double-layer capacitance), and R_s (solution resistance). Both experimental curves (point) and fitting curves (line) in the Nyquist plots are shown in Figure 4B. The R_{et} value of Pd/I:BiOBr-OV WE (curve b) is larger than that of bare WE (curve a). After modification of Ab_1, BSA, cTnI, and dAb-SOD-Au@PANI, the R_{et} increased

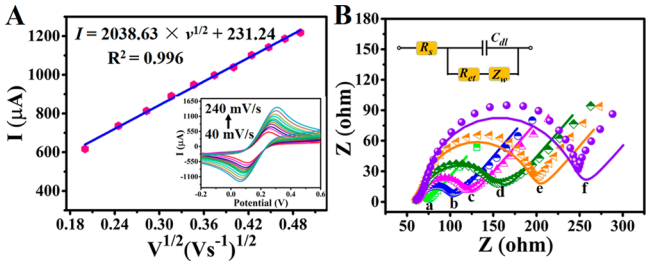

Figure 4. (A) Calibration curve of I against $\nu^{1/2}$ (inset shows the CV curves of response of Pd/I:BiOBr-OV electrodes at scan rates of 40−240 mV s^{-1}). (B) EIS characterization of each interfacial properties for the developed microfluidic cathodic PEC biosensor.

gradually, which demonstrated the successful decoration of each interfacial layer.

3.5. Analytical Performance of the Fabricated Biosensor. Based on the excellent PEC performance of Pd/I:BiOBr-OVs as a sensing substrate for cAb incubation and signal amplification of SOD-Au@PANI as a label, a sensitive biosensor was fabricated for the detection of cTnI. Under the optimal experimental parameters (Figure S8A,B), the PEC signal enhanced gradually along with the increasing concentration of cTnI within the range from 0.1 pg/mL to 100 ng/mL (from curve a to curve g), as shown in Figure 5A. As a result, a good linear in correlation was achieved between PEC intensity and logarithm of different cTnI concentrations (log c), as shown in Figure 5B. The calibration plot was obtained as $y = -0.4794 \times \log c - 3.3428$ with a correlation coefficient $R^2 = 0.996$. In addition, the limit of detection was calculated to be 0.042 pg/mL. Moreover, compared with the existing detection methods in previous work (Table S1), this proposed biosensor exhibited superior analytical performance for cTnI detection.

Specificity was essential for assessment selectivity of the designed PEC biosensor. The interference concentration (PSA, PCT, and Aβ) was selected as 10 and 1000 ng/mL, respectively, which were 100 times higher than that of 0.1 and 10 ng/mL for target cTnI. As shown in Figure 5C, compared to the PEC intensity of the blank group, the PEC intensities of these interferences exhibited barely negligible changes. Importantly, the PEC intensities of the mixture targets (PSA + cTnI, PCT + cTnI, and Aβ + cTnI) were almost the same as pure cTnI, indicating that the fabricated biosensor had a satisfactory specificity without obvious interference. In addition, the reproducibility can be evaluated by comparing PEC intensities among various electrodes. As displayed in Figure 5D, the six parallel identical electrodes were modified with 10 ng/mL (number 1−6) and 0.1 ng/mL (number 1−6) cTnI in a double-channel biosensor and carried out the PEC intensity, respectively, in which the RSD was calculated to be 1.36 and 1.82%, respectively. The results illustrated that the prepared PEC biosensor has an acceptable reproducibility. Simultaneously, the fabricated biosensor presented good stability, as shown in Figure S9.

3.6. Real-Sample Analysis. To validate the feasibility and accuracy of the designed biosensor, a recovery test based on the standard addition method was carried out in two healthy human serum samples by spiking different concentrations of target cTnI (0.1, 5, and 30 ng/mL). It could be seen from Table 1 that recoveries of the prepared biosensor ranged from 98.3 to 101.8% with an RSD value from 1.38 to 2.49% for sample 1 and 97.0 to 103.5% with an RSD value from 1.53 to

https://doi.org/10.1021/acs.analchem.1c02922
Anal. Chem. 2021, 93, 14196−14203

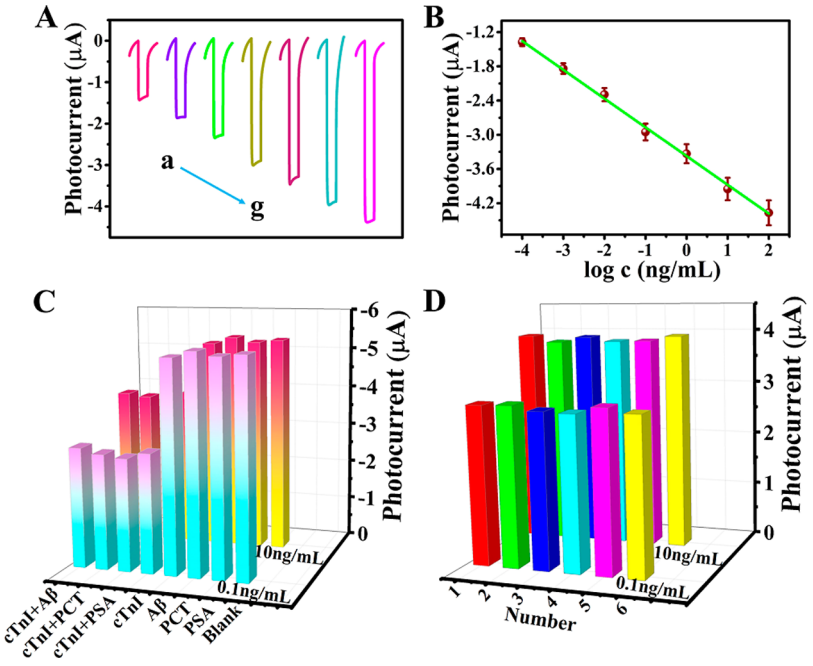

Figure 5. (A) Cathodic PEC responses of the proposed biosensor toward various concentrations of cTnI from 0.1 pg/mL to 100 ng/mL (a−g); (B) linear relationship between photocurrent and logarithm of different cTnI concentrations; (C) specificity of the developed biosensor for over other interfering antigens, including PSA (10, 1000 ng/mL), PCT (10, 1000 ng/mL), and Aβ (10, 1000 ng/mL) and their mixture. (D) Reproducibility of the developed biosensor for cTnI (0.1, 10 ng/mL) detection in the same batch.

Table 1. Real-Samples Analysis of cTnI in Healthy Human Serum Samples

sample	spiked (ng/mL)	found (ng/mL)	RSD (%)	recovery (%)	sample	spiked (ng/mL)	found (ng/mL)	RSD (%)	recovery (%)
1	0	0.036			2	0	0.127		
	0.10	0.137	2.49	101		0.10	0.224	3.32	97.0
	5.0	4.95	1.79	98.3		5.0	5.304	1.53	103.5
	30	30.6	1.38	101.8		30	30.24	1.96	100.4

3.32% for sample 2, which proved that the developed biosensor was accurate and reliable for real-sample analysis.

4. CONCLUSIONS

In conclusion, an innovative and preferable double-channel microfluidic cathodic PEC biosensor has been developed on the basis of enhancing cathodic photocurrent response of Pd/I:BiOBr-OVs as a sensing platform and an amplifying signal of SOD-Au@PANI as a detection antibody label. The introduction of OVs and Pd on the surface of I:BiOBr can effectively enhance cathodic PEC performance owing to the improvement of efficiency separation of photogenerated electron−hole pairs. Furthermore, the SOD on the signal amplification label of SOD-Au@PANI could catalyze generated $^{\bullet}O_2^-$ to produce H_2O and O_2. Then, the generated O_2 can capture photogenerated electrons for promoting the separation of electron−hole pairs to achieve the amplifying signal. The cathodic PEC biosensor integrated into a double-channel microfluidic template presents superiorities of high selectivity, rapid detection, and low cost and provides possibilities for detecting cTnI in human serum samples. Importantly, the designed cathodic PEC strategy has great potential application prospect for the detection of other targets in biological analysis and early disease diagnosis.

■ ASSOCIATED CONTENT

Supporting Information

The Supporting Information is available free of charge at https://pubs.acs.org/doi/10.1021/acs.analchem.1c02922.

Materials, apparatus, preparation of a three-microelectrode system in microfluidic by wet etching and silk screen printing, PDMS of the isolation membrane and double-channel microfluidic, HRTEM image of Pd/I:BiOBr-OVs, LSV measurement of BiOBr and I:BiOBr, CV and linear relation of I and $v^{1/2}$ for bare WE, optimized experimental parameters, and stability of the fabricated double-channel microfluidic cathodic PEC biosensor (PDF)

■ AUTHOR INFORMATION

Corresponding Authors

Yu Du − *Collaborative Innovation Center for Green Chemical Manufacturing and Accurate Detection, Key Laboratory of Interfacial Reaction & Sensing Analysis in Universities of Shandong, University of Jinan, Jinan 250022 Shandong, China;* orcid.org/0000-0002-9002-8845; Email: duyu_ujn@163.com

Hongmin Ma − *Collaborative Innovation Center for Green Chemical Manufacturing and Accurate Detection, Key Laboratory of Interfacial Reaction & Sensing Analysis in Universities of Shandong, University of Jinan, Jinan 250022*

https://doi.org/10.1021/acs.analchem.1c02922
Anal. Chem. 2021, 93, 14196−14203

Shandong, China; orcid.org/0000-0002-7061-8944; Email: mahongmin2002@126.com

Authors

Jinhui Feng − *Collaborative Innovation Center for Green Chemical Manufacturing and Accurate Detection, Key Laboratory of Interfacial Reaction & Sensing Analysis in Universities of Shandong, University of Jinan, Jinan 250022 Shandong, China*

Ning Li − *School of Information Science and Engineering, University of Jinan, Jinan 250022, China*

Xiang Ren − *Collaborative Innovation Center for Green Chemical Manufacturing and Accurate Detection, Key Laboratory of Interfacial Reaction & Sensing Analysis in Universities of Shandong, University of Jinan, Jinan 250022 Shandong, China;* orcid.org/0000-0002-4321-4282

Xueying Wang − *Collaborative Innovation Center for Green Chemical Manufacturing and Accurate Detection, Key Laboratory of Interfacial Reaction & Sensing Analysis in Universities of Shandong, University of Jinan, Jinan 250022 Shandong, China*

Xuejing Liu − *Collaborative Innovation Center for Green Chemical Manufacturing and Accurate Detection, Key Laboratory of Interfacial Reaction & Sensing Analysis in Universities of Shandong, University of Jinan, Jinan 250022 Shandong, China;* orcid.org/0000-0003-3644-0369

Qin Wei − *Collaborative Innovation Center for Green Chemical Manufacturing and Accurate Detection, Key Laboratory of Interfacial Reaction & Sensing Analysis in Universities of Shandong, University of Jinan, Jinan 250022 Shandong, China;* orcid.org/0000-0002-3034-8046

Complete contact information is available at: https://pubs.acs.org/10.1021/acs.analchem.1c02922

Author Contributions

[§]J.F. and N.L. contributed equally to this work.

Notes

The authors declare no competing financial interest.

■ ACKNOWLEDGMENTS

This study was supported by the National Key Scientific Instrument and Equipment Development Project of China (no. 21627809), Special Foundation for Taishan Scholar Professorship of Shandong Province, Jinan Scientific Research Leader Workshop Project (2018GXRC024 and 2018GXRC021), the National Natural Science Foundation of China (no. 21777056), and Innovation Team Project of Colleges and Universities in Jinan (no. 2019GXRC027).

■ REFERENCES

(1) Hu, D.; Liang, H.; Wang, X.; Luo, F.; Qiu, B.; Lin, Z.; Wang, J. *Anal. Chem.* **2020**, *92*, 10114−10120.
(2) Guan, X.; Deng, X.; Song, J.; Wang, X.; Wu, S. *Anal. Chem.* **2021**, *93*, 6763−6769.
(3) Feng, J.; Qian, Y.; Cheng, Q.; Ma, Y.; Wu, D.; Ma, H.; Ren, X.; Wang, X.; Wei, Q. *Biosens. Bioelectron.* **2020**, *168*, 112503.
(4) Martín, A.; Kim, J.; Kurniawan, J. F.; Sempionatto, J. R.; Moreto, J. R.; Tang, G.; Campbell, A. S.; Shin, A.; Lee, M. Y.; Liu, X.; Wang, J. *ACS Sens.* **2017**, *2*, 1860−1868.
(5) Feng, J.; Wu, T.; Cheng, Q.; Ma, H.; Ren, X.; Wang, X.; Lee, J. Y.; Wei, Q.; Ju, H. *Lab Chip* **2021**, *21*, 378−384.
(6) Feng, J.; Dai, L.; Ren, X.; Ma, H.; Wang, X.; Fan, D.; Wei, Q.; Wu, R. *Anal. Chem.* **2021**, *93*, 7125−7132.
(7) Liu, Y.-L.; Zhu, Y.-C.; Qu, L.-B.; Yang, R.; Yu, X.-D.; Zhao, W.-W. *ACS Appl. Bio Mater.* **2019**, *2*, 2703−2707.
(8) Wang, H.; Zhang, B.; Zhao, F.; Zeng, B. *ACS Appl. Mater. Interfaces* **2018**, *10*, 35281−35288.
(9) Ma, H.; Ma, W.; Chen, J.-F.; Liu, X.-Y.; Peng, Y.-Y.; Yang, Z.-Y.; Tian, H.; Long, Y.-T. *J. Am. Chem. Soc.* **2018**, *140*, 5272−5279.
(10) Gao, B.; Zhao, X.; Liang, Z.; Wu, Z.; Wang, W.; Han, D.; Niu, L. *Anal. Chem.* **2021**, *93*, 820−827.
(11) Kim, D. S.; Kim, Y. B.; Jung, S. H.; Deshpande, N. G.; Choi, J. H.; Lee, H. S.; Cho, H. K. *J. Mater. Chem. A* **2020**, *8*, 21744−21755.
(12) Han, Q.; Zhao, X.; Na, N.; Ouyang, J. *Anal. Chem.* **2021**, *93*, 3486−3492.
(13) Wei, H. Y.; Zhang, H. Y.; Zhang, W. M.; Wang, S. M.; Xiao, J. Y.; Cui, T.; Bai, Y. P.; Niu, H. S.; Li, T. T.; Li, X. W. *Adv. Mater. Res.* **2015**, *1088*, 33−37.
(14) Yu, W.; Yin, J.; Li, Y.; Lai, B.; Jiang, T.; Li, Y.; Liu, H.; Liu, J.; Zhao, C.; Singh, S. C.; Chen, J.; Lin, B.; Idriss, H.; Guo, C. *ACS Appl. Energy Mater.* **2019**, *2*, 2751−2759.
(15) Liu, J.; Zhang, X.; Zhong, Q.; Li, J.; Wu, H.; Zhang, B.; Jin, L.; Tao, H. B.; Liu, B. *J. Mater. Chem. A* **2020**, *8*, 4083−4090.
(16) Geng, Y.; Chen, D.; Li, N.; Xu, Q.; Li, H.; He, J.; Lu, J. *Appl. Catal., B* **2021**, *280*, 119409.
(17) Yu, S.-Y.; Mei, L.-P.; Xu, Y.-T.; Xue, T.-Y.; Fan, G.-C.; Han, D.-M.; Chen, G.; Zhao, W.-W. *Anal. Chem.* **2019**, *91*, 3800−3804.
(18) Liang, L.; Gao, S.; Zhu, J.; Wang, L.; Yang, L. *Chem. Eng. J.* **2019**, *391*, 123599.
(19) Jin, J.; Wang, Y.; He, T. *RSC Adv.* **2015**, *5*, 100244−100250.
(20) Wang, H.; Zhang, B.; Wang, C.; Xi, J.; Zhao, F.; Zeng, B. *ACS Appl. Nano Mater.* **2020**, *3*, 6423−6431.
(21) Wu, J.; Li, X.; Shi, W.; Ling, P.; Sun, Y.; Jiao, X.; Gao, S.; Liang, L.; Xu, J.; Yan, W.; Wang, C.; Xie, Y. *Angew. Chem., Int. Ed.* **2018**, *130*, 8855−8859.
(22) Li, H.; Shang, J.; Ai, Z.; Zhang, L. *J. Am. Chem. Soc.* **2015**, *137*, 6393−6399.
(23) Zheng, C.; Cao, C.; Ali, Z. *Phys. Chem. Chem. Phys.* **2015**, *17*, 13347−13354.
(24) Li, P.; Zhou, Z.; Wang, Q.; Guo, M.; Chen, S.; Low, J.; Long, R.; Liu, W.; Ding, P.; Wu, Y.; Xiong, Y. *J. Am. Chem. Soc.* **2020**, *142*, 12430−12439.
(25) Chen, X.; Zhang, X.; Li, Y.; Qi, M.; Xu, Y. *Appl. Catal., B* **2021**, *281*, 119516.
(26) Li, X.; Wang, T.; Tao, X.; Qiu, G.; Li, C.; Li, B. *J. Mater. Chem. A* **2020**, *8*, 17657−17669.
(27) Feng, J.; Li, F.; Li, X.; Wang, Y.; Fan, D.; Du, B.; Li, Y.; Wei, Q. *Biosens. Bioelectron.* **2018**, *117*, 773−780.
(28) Hao, L.; Huang, H.; Zhang, Y.; Ma, T. *Adv. Funct. Mater.* **2021**, *31*, 2100919.
(29) Zhang, X.; Pei, C.; Chang, X.; Chen, S.; Liu, R.; Zhao, Z.-J.; Mu, R.; Gong, J. *J. Am. Chem. Soc.* **2020**, *142*, 11540−11549.
(30) Song, D.; Zheng, J.; Myung, N.; Xu, J.; Zhang, M. *Talanta* **2021**, *225*, 122006.
(31) Jia, W.; Peng, D.; Feng, Z.; Wu, X.; Liu, Y.; Zheng, X.; Yuan, X. *New J. Chem.* **2020**, *44*, 7749−7757.
(32) Yang, X.; Zhang, X.; Wu, T.; Gao, P.; Zhu, G.; Fan, J. *Colloids Surf., A* **2020**, *605*, 125344.
(33) Wu, D.; Yue, S.; Wang, W.; An, T.; Li, G.; Yip, H. Y.; Zhao, H.; Wong, P. K. *Appl. Catal., B* **2016**, *192*, 35−45.
(34) Lin, Y.; Liu, H.; Yang, C.; Wu, X.; Zhong, Y. *Appl. Catal., B* **2020**, *264*, 118479.